Journal of Power Sources 681 (2026) 240293

Contents lists available at ScienceDirect

Journal of Power Sources

journal homepage: www.elsevier.com/locate/jpowsour

DRT-based impedance analysis of two-phase flow conditions in PEM water electrolyzer cells

Debora Brinker [a,*], Niklas Hensle [a,b], Christin Büsching [a], David Breuninger [a], Tom Smolinka [b], André Weber [a,*]

[a] Institute for Applied Materials (IAM-ET), Karlsruhe Institute of Technology (KIT), Adenauerring 20b, Karlsruhe, 76131, Germany
[b] Fraunhofer Institute for Solar Energy Systems ISE, Heidenhofstrasse 2, Freiburg, 79110, Germany

HIGHLIGHTS

- Incremental cell approach enables localized two-phase flow emulation.
- Oxygen addition to anode stream shows negligible impact on resistance.
- Higher gas amounts raise HFR, likely from cathode-side membrane dehydration.
- Low currents show reduced polarization resistance due to added cathode hydrogen.
- Comparison of incremental and along-channel cells approach.

ARTICLE INFO

Keywords:
Electrochemical impedance spectroscopy
Distribution of relaxation times
Incremental test cell
Along-the-channel test cell
Gas injection
Two-phase flow

ABSTRACT

The accumulation of hydrogen and oxygen within the flow channels of proton exchange membrane water electrolysis cells results in increased gas fractions and pronounced two-phase flow effects at higher current densities. Spatially resolved segmentation along the channel permits investigation of such gradients but necessitates complex hardware. In this study, a simplified method is introduced to emulate local gas production in an incremental cell through controlled injection of well-defined amounts of hydrogen and oxygen into the respective inlet streams. The impact of the gas-to-water ratio on ohmic resistance and polarization phenomena is examined using electrochemical impedance spectroscopy combined with subsequent distribution of relaxation times analysis. This reveals membrane dehydration effects as well as an impact on activation-related losses on the cathode side. A detailed comparison between an incremental (zero gradient) cell and an along-the-channel cell demonstrates a good overall performance correlation. In the medium current density region (2-3 A cm^{-2}), the along-the-channel cell shows significantly increased polarization losses, which might be attributed to contamination from ion release from the CCM and/or mass transport issues.

1. Introduction

Green hydrogen is widely recognized as a key energy carrier for the decarbonization of both industrial processes and the transport sector [1], [2], [3]. Among the available technologies, proton exchange membrane (PEM) water electrolysis enables the production of high-purity hydrogen while offering high efficiency, compact system design, and the ability to operate dynamically in combination with fluctuating renewable energy sources [4], [5], [6], [7]. However, large-scale deployment of PEM water electrolysis requires significant upscaling of cell and stack dimensions as well as operation at increasingly high current densities [8], [9], [10].

Recent developments in membrane electrode assembly (MEA) design, particularly the use of thinner membranes and optimized catalyst layers, have enabled stable operation at current densities well beyond today's conventional industrial conditions [9], [10], [11]. While these advances are essential for reducing system costs and increasing hydrogen production rates, they simultaneously intensify mass transport challenges within the cell. With increasing active area and current density, the local generation rates of hydrogen and oxygen rise

---

* Corresponding author.
E-mail addresses: debora.brinker@kit.edu (D. Brinker), andre.weber@kit.ed (A. Weber).

https://doi.org/10.1016/j.jpowsour.2026.240293
Received 11 March 2026; Received in revised form 29 April 2026; Accepted 30 April 2026

drastically, leading to high gas fractions in the porous transport layers and flow channels.

These two-phase flow conditions can influence the cell performance. Investigations into this behavior primarily employ optical methods and focus on bubble formation [12]. Majasan et al. [13] explore the effects of varying parameters on cell performance. They showed that the flow-field design affects the two-phase flow behavior. Ito et al. [14] showed that, in slug and annular flow regimes at the anode, water mass transport is hindered, leading to increased mass transport losses at high current densities.

Against this background, the targeted adjustment of defined gas fractions in the inlet flow is a suitable approach to controllably replicate characteristic two-phase conditions, such as those occurring in downstream regions of along the channel cells. This allows the influence of increased gas fractions on impedance behavior and polarization losses to be investigated in isolation, without simultaneously superimposing geometrically induced gradients along the channel direction.

To address the resulting spatial gradients within large-sized PEM water electrolyzer cells and stacks, several research groups have developed segmented along the channel (AtC) test cells, which enable spatially resolved electrochemical analysis along the flow direction [15], [16], [17], [18]. These cells typically feature long channels combined with a narrow active width, allowing the investigation of gradients in current density, temperature, and impedance along the channel length. Using such experimental setups, significant variations could be observed along the channel, especially at high current density and low water flow rate, which suggests water starvation phenomena [19].

While AtC cells provide invaluable insights into spatially resolved behavior, they also come with considerable experimental complexity. The segmented design requires sophisticated electrical insulation, homogenous contact of the individual segments, and complex data acquisition systems. Furthermore, such setups are limited to specialized laboratory environments and are not easily adaptable for systematic parameter studies or routine diagnostic measurements.

As a result, there remains a strong demand for simplified experimental approaches that are able to reproduce local operating conditions in a large-sized cell, including two-phase flow-related effects, while retaining the experimental efforts of small-scale single cells.

Incremental single cells exhibiting an active electrode are of about 1 cm^2 can be operated under zero gradient conditions enabling a well-defined electrochemical environment required for fundamental investigations using techniques such as electrochemical impedance spectroscopy (EIS). EIS and the subsequent impedance data analysis by the distribution of relaxation times (DRT) has emerged as a powerful diagnostic tool for PEM water electrolysis in recent years. This approach enabled the deconvolution and quantification of different loss contributions related to ohmic, charge transfer, and mass transport phenomena [20], [21], [22], [23].

However, due to their limited active area, the absolute amount of gas produced in such incremental cells is comparatively low, limiting their ability to reproduce gas-transport and two-phase flow related phenomena, unavoidable in technically relevant cell sizes.

To bridge this gap, the intentional injection of well-defined amounts of hydrogen and/or oxygen into the respective inlet streams of an incremental PEM water electrolysis cell represents a promising approach to mimic the gas production of the upstream cell area of a large scale cell and thus enables a replication of local operating conditions in large scale stacks. To the best of our knowledge, no such strategy has yet been reported for PEM water electrolysis.

In this study, electrochemical impedance spectroscopy combined with distribution of relaxation times (DRT) analysis is employed to investigate the impact of well-defined two-phase flow conditions in an incremental PEM water electrolysis cell [24]. By systematically varying the injected gas amounts, two-phase flow conditions representing different positions along the channel of a large-scale cell are mimicked, and the influence of the gas-to-water ratio on ohmic resistance and polarization phenomena is examined. This approach of mixing gases to the water supplied to an incremental cell enables studies at well-defined gas to water ratios. Thus, a local condition in a large cell/stack can be mimicked and the local cell performance can be determined, providing essential parameters for modeling two-phase flow effects on the stack level.

The results of the incremental cell are compared with those from a segmented along-the-channel PEM water electrolyzer cell. This comparison aims to assess the extent to which controlled gas injection can reproduce locally resolved electrochemical behavior, thereby providing a simplified experimental alternative for studying two-phase flow-related effects in PEM water electrolysis.

2. Experimental

2.1. Test cells

Two distinct test cells, specifically the incremental (Inc) test cell of KIT and the AtC test cell of Fraunhofer ISE, were utilized in this study as shown in Fig. 1 a) and b), respectively. Both are in-house developed test cells and have been described in detail elsewhere [15], [24]. This study emphasizes that the AtC cell comprises a segmented cell with ten independent segments aligned along the flow direction. Each segment measures 2 cm in width and 2.8 cm in length. Temperature and current measurements can be obtained independently for each segment. The incremental cell features an active area of 2.1 cm^2, with dimensions of 1.4 cm in width and 1.5 cm in length. Its compact size facilitates uniform operating conditions across the entire cell surface. Both test cells incorporate identical channel and rib structures, with parallel channels measuring 2 mm in depth and 1 mm in width. The land area is 0.9 mm wide. For this research, CCMs were fabricated from commercially available materials at Fraunhofer ISE. The membrane utilized is Nafion N115. The anode catalyst loading is approximately 0.5 mg$_{\mathrm{Ir}}$/cm^2, the catalyst (Premion, 99.99%, 84.5% Iridium (IV) oxide) is provided by *ThermoFisher Scientific, Germany* and the ionomer (Nafion D2020) by *Ion Power GmbH, Germany*, with an ionomer to solid ratio of 16.68% The cathode catalyst loading is approximately 0.25 mg$_{\mathrm{Pt}}$/cm^2, the catalyst (Elyst Pt50 0550, 50% Pt) is provided by *Umicore AG & Co. KG, Germany* and the ionomer (Aquivion D79) by *Sigma-Aldrich, USA*, with an ionomer to solid ratio of 29.75%. The anode catalyst layer was screen printed onto ETFE foil, while the cathode catalyst layer was slot-die coated onto PTFE foil. Both catalyst layers were then hot pressed onto the membrane at 160 °C for 10 min under a force of 10 kN. Titanium-based materials from *NV Bekaert SA* (type 2GDL06-0.25) were employed as the porous transport layers (PTLs) on both sides.

2.2. Test benches

Regarding the measurements presented in this contribution, two distinct test benches were utilized at the two locations, KIT and Fraunhofer ISE. At Fraunhofer ISE, the along-the-channel cell was evaluated, while at KIT, the incremental cell was examined. At both sites, in-house-developed test benches were employed, which have already been documented in previous publications [24], [25], [26]. Both test benches provide the necessary operating conditions for the electrochemical measurements conducted in this study. Each is equipped with electrochemical workstations from *Zahner Elektrik GmbH & Co. KG, Germany*, capable of delivering currents up to 40 A. At both test benches, the water flow to the anode and cathode can be independently regulated. The measurements in this study involved a cathode without water circulation. Water quality is maintained through ion exchangers. The water can be heated and its temperature precisely controlled. Furthermore, the test bench at KIT allows for the heating of the test cell itself via heating cartridges. Additionally, the KIT test bench is equipped with the capability to introduce gases into the inlet streams, which is essential for the measurements performed in this study. A detailed

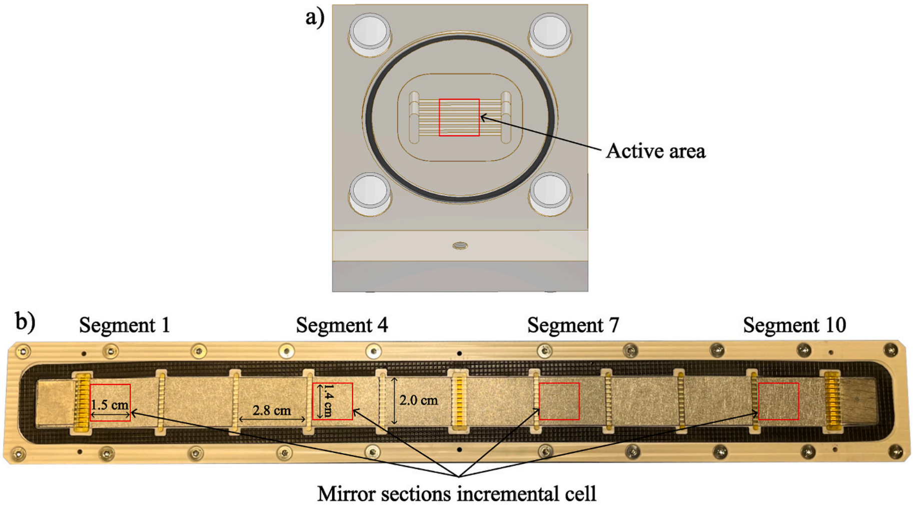

Fig. 1. Top view of the open a) Incremental test cell from KIT with active area marked in red, b) Along the channel test cell from the Fraunhofer ISE showing the sections mirrored by incremental test cell marked in red. (For interpretation of the references to colour in this figure legend, the reader is referred to the Web version of this article.)

description of the setup will be provided in the subsequent section.

2.3. *Methodology for mimicking along-the-channel gas production in an incremental test cell*

In segmented AtC PEM water electrolysis cells, hydrogen and oxygen are generated locally in each segment and continuously accumulate along the flow direction. As a result, the gas fraction in the reactant streams increases progressively from the inlet toward the outlet of the cell. To reproduce these locally varying gas production conditions in a simpler and experimentally more accessible setup, the incremental test cell, introduced in Section 2.1, is employed. Instead of generating large amounts of product gases electrochemically, defined amounts of hydrogen and oxygen are externally injected into the inlet streams, allowing the gas fractions observed at specific locations in the AtC cell to be mimicked. In this way, the influence of gas accumulation on electrochemical performance can be studied independently of spatial gradients in current density or temperature.

In the experimental setup at the test bench at KIT water and gases are supplied from the one side of the cell. On the anode side, liquid water is mixed with oxygen, while on the cathode side only dry hydrogen is supplied. The two-phase mixtures exit the cell on the other side and are directed to gas–water separators, where the gas phase is removed and the liquid water is recirculated.

The AtC cell used for comparison consists of ten equally sized segments along the flow channel, as illustrated in Fig. 1 b). To represent different positions along the channel, four segments were selected for detailed comparison: Segment 1, Segment 4, Segment 7, and Segment 10, which are marked in red in Fig. 1 b). For each selected segment, the gas composition at the beginning of the segment was used as the reference condition, since the cumulative amount of gas produced upstream can be calculated.

The gas production in the AtC cell was determined based on Faraday's law in combination with the ideal gas law. The volumetric hydrogen flow rate at the beginning of segment i, $\dot{V}_{H_2,i}$, is calculated according to Equation (1).

$$\dot{V}_{H_2,i} = \dot{V}_{H_2,i-1} + \frac{I_i \cdot R \cdot T_i}{z \cdot F \cdot p} \tag{1}$$

Here $\dot{V}_{H_2,i-1}$ is the hydrogen volume flow entering the previous segment. For Segment 1, this value is set to zero. I_i denotes the current of segment i, T_i the corresponding segment temperature, $z = 2$ the number of electrons transferred per hydrogen molecule, F the Faraday constant, R the universal gas constant, and p the operating pressure, which was ambient pressure for all measurements in this study.

Based on the calculated hydrogen flow rate, the corresponding oxygen flow rate is obtained from reaction stoichiometry. Since half as much oxygen is produced as hydrogen, the oxygen volumetric flow rate is given by Equation (2).

$$\dot{V}_{O_2} = \frac{1}{2} \cdot \dot{V}_{H_2,i} \tag{2}$$

The remaining water flow along the channel was calculated by accounting for both the electrochemically consumed water and the water transported through the membrane by electro-osmotic drag. The water volume flow rate at the beginning of segment i is expressed by Equation (3) [27].

$$\dot{V}_{H_2O,i} = \dot{V}_{H_2O,i-1} - \frac{I_i \cdot M_{H_2O} \cdot (1 + n_{Drag})}{z \cdot F \cdot \rho_{H_2O}} \tag{3}$$

Here M_{H_2O} is the molar mass of water, ρ_{H_2O} its density, and n_{Drag} the electro-osmotic drag coefficient, which was assumed to be constant and independent of membrane humidification, temperature and pressure in this study. In the literature a wide range of electro-osmotic drag coefficient exists taking different factors into account, suggesting values between $0.9 < n_{Drag} < 7$ [28], [29]. For this study $n_{Drag} = 3$ was selected as a compromise. Diffusion and hydraulic permeation are neglected in this calculation. Overall, the calculated water consumption is negligible (<4 %) compared to the supplied water flow under the investigated industry relevant conditions. The current I_i measured for each segment of the AtC cell was used directly for the calculation.

To ensure identical flow velocities of 0.25 m s^{-1}, the inlet water flow rate of the AtC cell was adjusted to the incremental test cell by accounting for the different cell widths. While the AtC cell was operated with an inlet water flow rate of 300 mL min^{-1}, the width of the incremental cell corresponds to 70 % of the AtC cell width, resulting in an inlet water flow rate of 210 mL min^{-1} for the incremental test cell. All calculated gas and water flow rates used for the measurements presented in this work are summarized in Table SI1 in the Supplementary Information.

2.4. *Measurement methods*

In this study, we employ polarization curve measurements, electrochemical impedance spectroscopy, and the subsequent distribution of relaxation times analysis. The polarization curves are measured from 0.01 A cm^{-2} to 7 A cm^{-2}, with varying step sizes and a 2 min holding time.

Electrochemical impedance measurements are conducted across current densities ranging from 0.1 A cm^{-2} to 7 A cm^{-2}. The cell undergoes stabilization at each new current density for a minimum of 15 min prior to the EIS measurement. The measurement is executed with an amplitude set at 10% of the direct current bias. Impedance spectra are obtained over a frequency range from 100 kHz to 100 mHz, utilizing a frequency resolution of 10 steps per decade and an integration time spanning 10 periods.

Data quality and LTI conditions were verified through the application of the Kramers-Kronig test to the impedance data. This method utilizes the relationship between the real and imaginary components of the impedance spectrum to assess causality, linearity, and time-invariance of the measurement. In this study, we use the method outlined by Schönleber et al. [30], which employs a Kramers-Kronig-compliant model in which a series connection of RC elements is fitted to the measured data. The quality of the measured data can subsequently be evaluated based on the residual. For this investigation, residual <2% were obtained. Invalid data in the high-frequency region (>50 kHz) was excluded from further analysis.

The distribution of relaxation times analysis facilitates a more detailed investigation into the ongoing polarization processes. These processes are more distinctly separated by their characteristic time constants. For this purpose, Equation (4) is employed [31].

$$Z(\omega) = R_0 + \int_0^\infty \frac{g(\tau)}{1 + j\omega\tau} d\tau \tag{4}$$

$Z(\omega)$ is the impedance and its distribution function $g(\tau)$ of relaxation times τ with R_0 the ohmic resistance of the spectrum. For the calculation of the DRT in this study, a numerical approach is used, based on a fit to the real part of the impedance spectrum. To include the negative inductive processes at low frequencies, an adaptation of this DRT calculation by Schiefer et al. [32] was used. Typically, only positive resistance and capacity values are used for the DRT calculation. In this adaptation, negative values were allowed in certain parts of the spectrum representing a physicochemical meaningful resistance decay. It is thereby assumed, that the inductive processes leady to a delayed improvement in cell performance. As a stabilization method for the DRT calculation, the Tikhonov regularization [33] is used. A regularization parameter λ of 0.005 was used for all DRTs shown in this study.

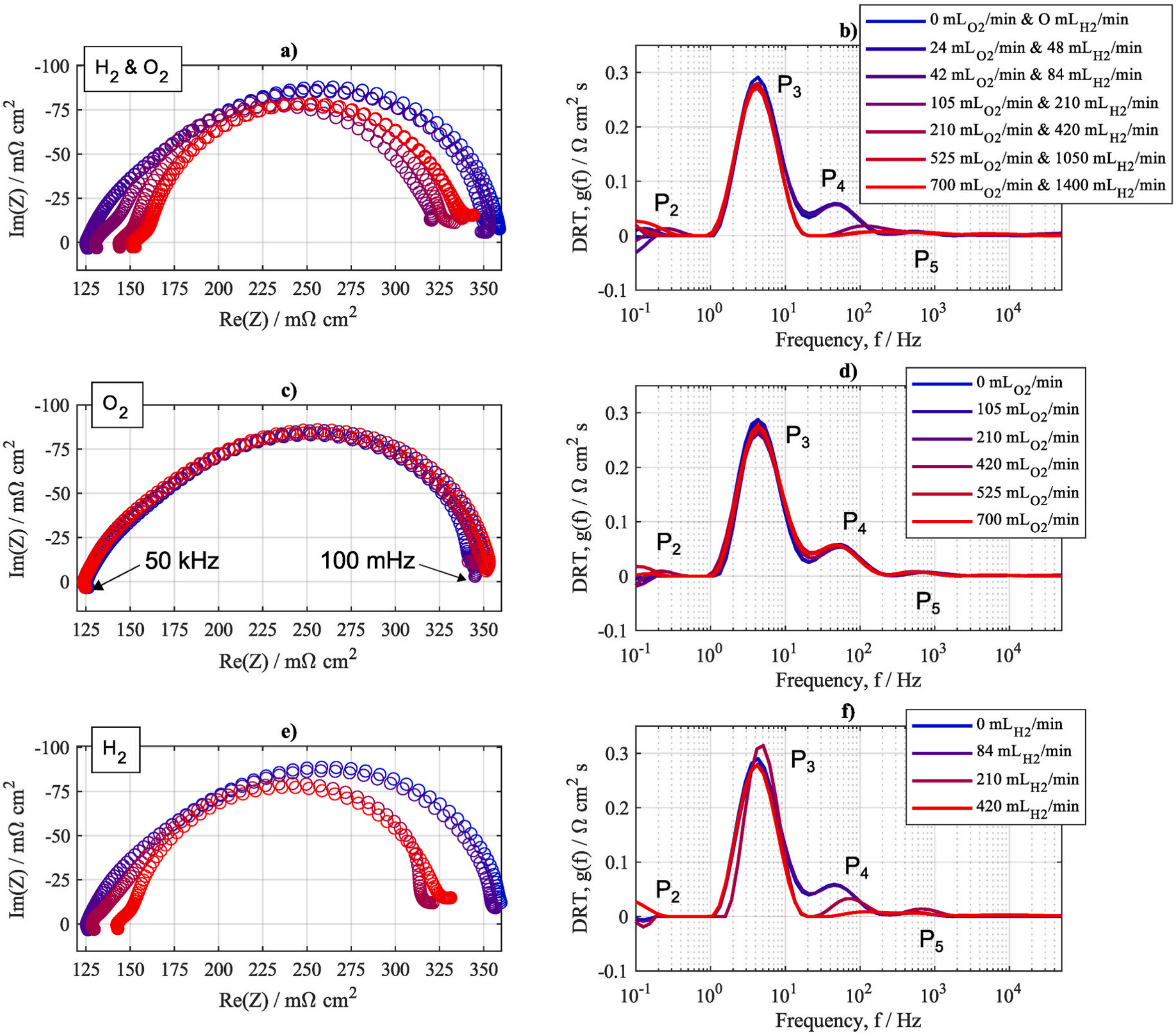

Fig. 2. The Nyquist and DRT spectra for the gas mixing in the incremental test cell with supply of a) and b) both hydrogen and oxygen, c), d) only oxygen to the anode, e), f) only hydrogen to the cathode at 100 mA cm^{-2}.

3. Results

3.1. Gas injection variation

Initially, the gas mixing process involves introducing gases into the inlet streams of the incremental test cell, generally through varying the quantities supplied and the manner of supply, either at both sides or at a single side. The gases are consistently supplied to the side where they are produced; thus, hydrogen is supplied to the cathode and/or oxygen to the anode. The results for two different current densities, specifically 0.1 A cm^{-2} and 2 A cm^{-2}, are presented in Figs. 2 and 3, respectively. In both figures the Nyquist and DRT spectra are shown with a) and b) depicting the mixing of both oxygen and hydrogen, c) and d) illustrating mixing of only oxygen, and e) and f) depicting mixing of only hydrogen. A total of eight different quantities of gases have been supplied, as detailed in Table SI2 (in the supplementary information), ranging from 0 mL min^{-1} to 700 mL_{O2} min^{-1} or 1400 $mL_{H2}min^{-1}$, respectively. The amount of hydrogen supplied is twice that of oxygen, aligning with the expected behavior in the reaction. The water volume percentage at the beginning of the cell varies from 100% down to 3%, as also documented in Table SI2.

In our previous investigation [24], we have looked into the behavior of the different peaks in the DRT and their dependency on operation parameter changes. Five capacitive peaks and one inductive peak could be separated. The low-frequency inductive peak P_{ind} (<1 Hz) depends on current density, temperature, and pressure. It becomes only visible at elevated current density (>2 A cm^{-2}). The peaks P_1 and P_2 (0.1–200 Hz) only become visible at higher current density and increase with it. Therefore, they are likely related to mass transport, though their specific association remains unclear. P_3 dominates at low current densities and decreases at higher ones, suggesting a link to charge-transfer kinetics of the OER which might be overlapped by HER-related processes. The high-frequency peaks P_4 and P_5 (>100 Hz) are deemed to be side peaks of P_3, arising from coupled charge-transfer and proton-transport processes in the ionomer resulting in such transmission-line-model behavior. Additionally, P_4 may be influenced by faster HER kinetics.

Fig. 2 illustrates that at low current density (specifically at 0.1 A cm^{-2}), for measurements with no or minimal gas flow (up to 42 mL_{O2} min^{-1} and 84 mL_{H2} min^{-1}, respectively), the polarization resistance remains stable before experiencing a sudden decrease at the step to 105 mL_{O2} min^{-1} and 210 mL_{H2} min^{-1}. Subsequently, the polarization resistance stabilizes again. Examination of the DRT in Fig. 2 b) reveals a

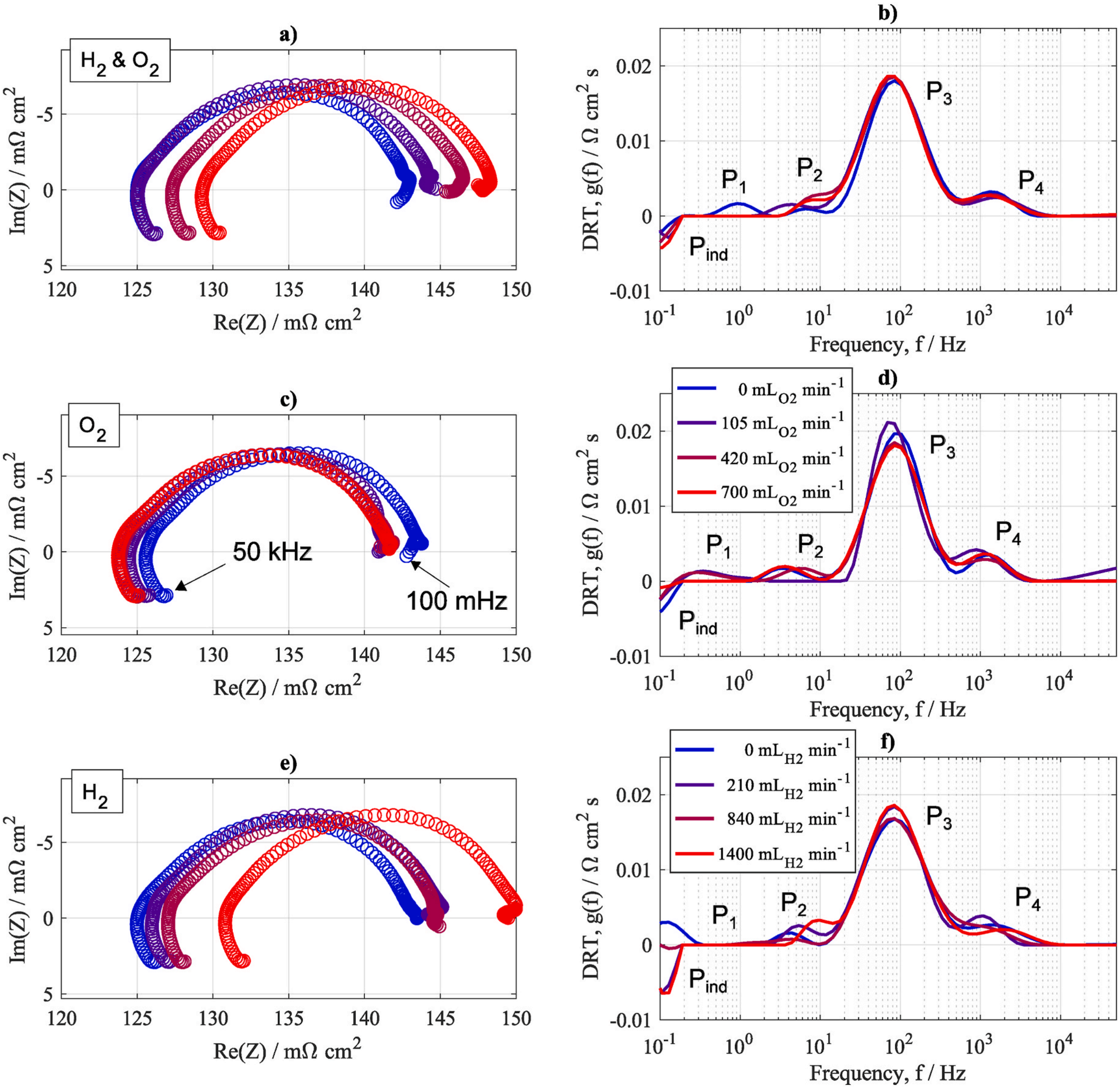

Fig. 3. The Nyquist and DRT spectra for the gas mixing in the incremental test cell with supply of a) and b) both hydrogen and oxygen, c), d) only oxygen to the anode, e), f) only hydrogen to the cathode at 2 A cm^{-2}, 60 °C, 0 bar, and a water flow rate of 10 mL min^{-1} cm^{-2} at the anode side.

reduction peak P_4 at around 60 Hz. The dominant peak P_3 at 5 Hz remains unaffected by this behavior. This phenomenon may suggest an activation effect, whereby sufficient product gas presence results in a decreased polarization resistance. To investigate whether this behavior is associated with oxygen or hydrogen, the gases were supplied separately, as depicted in Fig. 2 c) and 2 d) for oxygen and Fig. 2 e) and 2 f) for hydrogen. It becomes apparent that oxygen supply does not influence the polarization processes. Conversely, hydrogen supply exhibits the same effect as previously described. Consequently, this phenomenon appears to be related to the hydrogen supply; however, it should not be interpreted as a direct acceleration of intrinsic HER rate constants. Rather, the presence of hydrogen likely modifies local interfacial conditions within the cathode catalyst layer, including gas–liquid distribution and ionomer hydration. Moreover, at low current densities—where the cathode operates close to equilibrium and HER and HOR may coexist—such changes can affect the effective balance between forward and backward reaction pathways [34]. This, in turn, can lead to a reduction of P_4, which reflects the coupled proton-transfer and charge-transfer resistance. The absence of corresponding changes in the low-frequency DRT region indicates that this effect is interfacial and/or kinetically coupled in nature, rather than associated with macroscopic mass-transport limitations.

Additionally, Fig. 2 a) indicates that the ohmic resistance is not constant but rather increases with higher gas flow rates. This increase could indicate membrane drying, leading to reduced membrane conductivity. Analyzing the individual gas supply scenarios confirms that oxygen supply has no impact; however, hydrogen supply shows a similar increase, suggesting that this issue lies on the cathode side. This is reasonable as, despite adequate water being supplied to the anode side, the cathode side of the membrane or ionomer may dry out, as insufficient water is transported through the membrane to replace that removed by the dry gas supply.

Fig. 3 illustrates the results of this gas supply variation at a current density of 2 A cm^{-2}. The configuration remains consistent with Fig. 3 a) and b) depicting the gas supply to both sides, c) and d) only oxygen supply, and e) and f) only hydrogen supply. In contrast to the low current density region, no evident impact on the polarization processes is observed at 2 A cm^{-2}, indicating that at higher current densities the electrochemical response is dominated by intrinsic gas generation and locally established two-phase flow conditions, thereby reducing the relative influence of externally supplied gas on interfacial transport.

Conversely, the ohmic resistance exhibits a similar trend to that observed at low current densities. In the case of dual-gas supply, an increase in ohmic resistance of approximately 5 mΩ cm^2 is observed with increasing gas quantity. For oxygen-only supply, the trend appears to be reversed, with a considerably smaller decrease of roughly 1 mΩ cm^2. This indicates, that there is still enough water present to prevent any dry-out effect. Possible explanations for this improvement could be that changes in anode-side two-phase flow might indirectly affect membrane hydration, interfacial water distribution, and/or local temperature. However, it should be noted that the trend is quite small and should not be overinterpreted. Regarding hydrogen-only supply, the trend reverts to that observed with dual-gas supply, showing an increase in ohmic resistance that is even more pronounced than when both sides are supplied with gas. This suggests that hydrogen supply to the cathode negatively impacts the ohmic resistance, potentially due to a local dry-out condition at the cathode side.

3.2. Entire cell comparison of incremental and AtC cell

To provide a more detailed analysis, we compare our incremental test cell with an along the channel test cell. Prior to evaluating the individual segments and the gas mixing process, a general comparison of the two test cells is presented. Fig. 4 displays the polarization curves of both cells. The dotted lines represent the HFR-free curves, where the HFR-related contribution has been subtracted from the cell voltage. The HFR value of was obtained from the EIS measurement at the same current density. It is observable that the voltage of the incremental cell is lower. In the HFR-free variant, the difference becomes considerably less pronounced, proving a higher ohmic resistance of the AtC cell that can be attributed to the additional components for segmentation (see Hensle et al. [15] for detailed information).

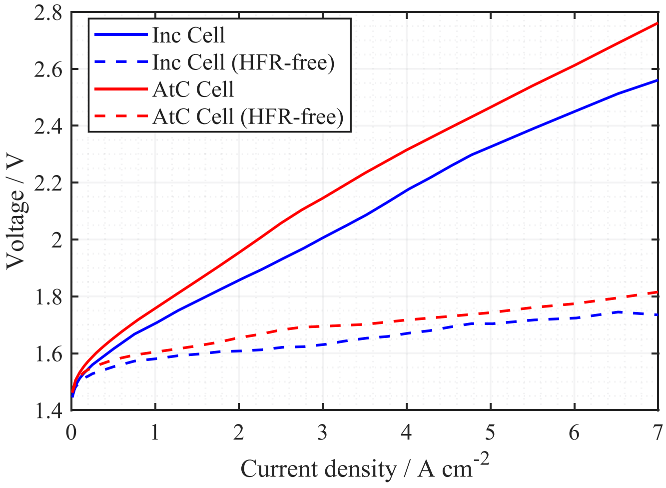

Fig. 4. Polarization curve of Inc and AtC cell including HFR free version of both at 60 °C, 0 bar and water flow rates of 10 mL min^{-1} cm^{-2} for the Inc cell and 5 mL min^{-1} cm^{-2} for the AtC cell.

Figs. 5 and 6 depict the Nyquist and DRT plots for the incremental cell, the entire AtC cell, and segment 1 of the AtC cell, across a current density range from 0.25 A cm^{-2} to 7 A cm^{-2}. The reduced ohmic resistance of the incremental cell is readily apparent, with an approximate value of 125 mΩ cm^2, in contrast to the AtC cell, which exhibits an ohmic resistance of approximately 150 mΩ cm^2 as can be seen in Fig. 5 a) for example. Similar trends between the different cells are observed concerning polarization resistance. Specifically, the polarization resistance diminishes with increasing current density up to 1 A cm^{-2} for the AtC cell and up to 2 A cm^{-2} for the incremental cell, as can be seen in Fig. 5 e) and Fig. 6 a), respectively. After this the polarization resistance begins to rise again, showing an increase in the low frequency region with new peaks P_1 and P_2 forming. Starting at 5 A cm^{-2} the formation of an inductive loop begins. The data for the entire cell and the initial segment of the AtC cell are highly comparable; however, the high-frequency data for the first segment are less precise than those of the entire cell, thereby complicating the determination of the ohmic resistance.

The DRT plots depicted in Fig. 5 for the lower current densities demonstrate a markedly similar behavior compared to each other. A prominent peak P_3 (starting around 10 Hz at low current density) diminishes as the current density increases. At elevated current densities, additional peaks P_1 and P_2 originating from the low-frequency region begin to form and intensify, along with an inductive peak P_{ind} at the low-frequency end. This phenomenon is observed in both test cells. These peaks have been ascribed to physico-chemical processes, as detailed in our previous publications [24], [35]. Briefly, peak P_3 that decreases with increasing current density within the medium frequency range is attributed to charge transfer kinetics, while the peaks P_1 and P_2 emerging at low frequency and high current density are associated with mass transport processes. From these observations, it is evident that the cells generally exhibit consistent trends with variations in current density and demonstrate comparable overall performance. Differences between the data of the entire AtC cell and the first segment are small, as expected. The strongest differences between the test cells can be seen at 2 A cm^{-2} and 3 A cm^{-2}, where the AtC cell shows a strong increase in overall polarization resistance, before decreasing again when the inductive loop starts to form. This behavior and possible origins will be

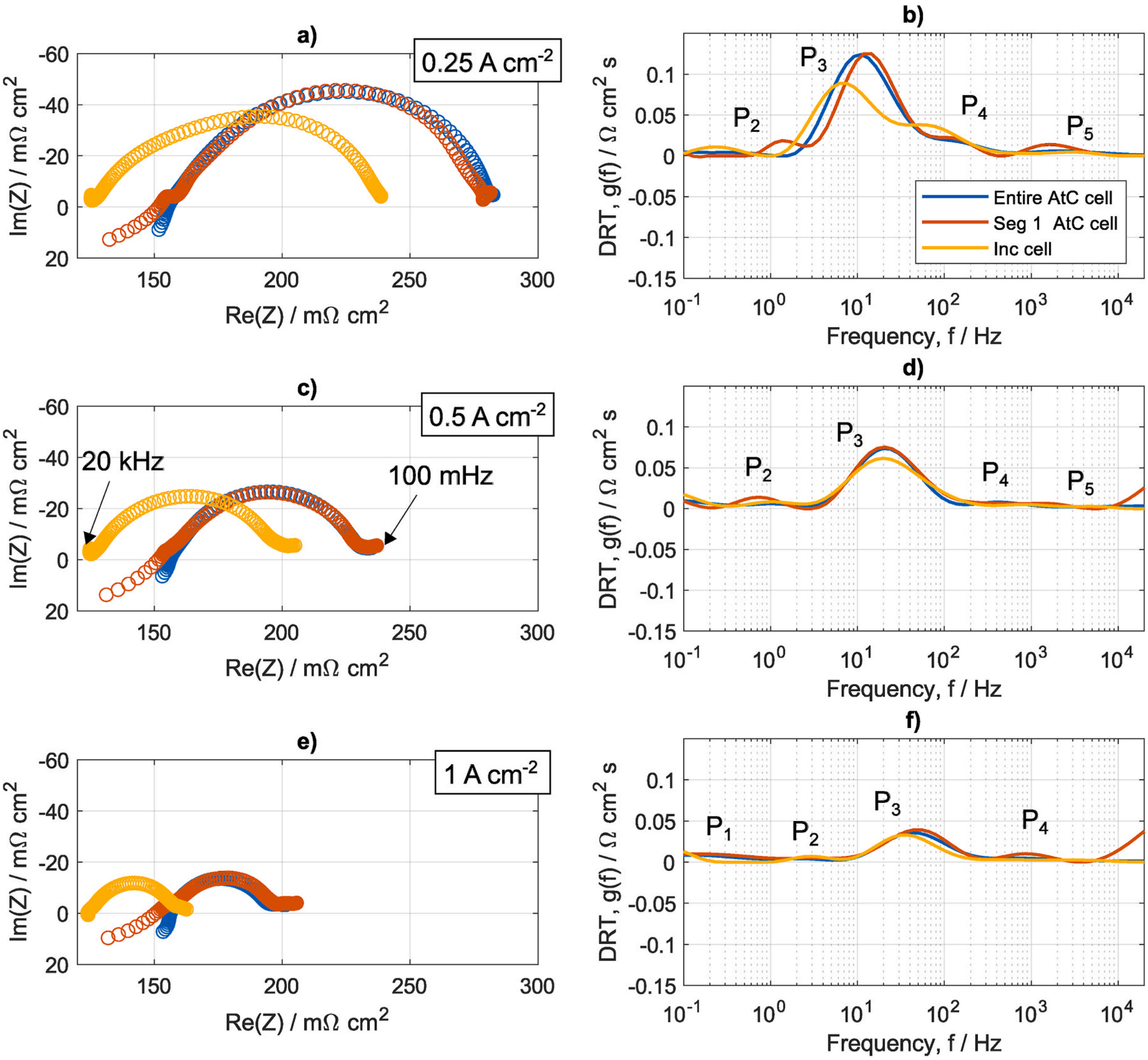

Fig. 5. Test cell comparison at low current densities of a), b) 0.25 A cm^{-2}, c) and d) 0.5 A cm^{-2}, and e) and f) 1 A cm^{-2} at 60 °C, 0 bar and water flow rates of 10 mL min^{-1} cm^{-2} for the Inc cell and 5 mL min^{-1} cm^{-2} for the AtC cell.

discussed further in the detailed comparison.

3.3. Comparison measurement data from AtC cell

Since the comprehensive evaluation of the two distinct test cells indicated a high degree of comparability, the subsequent step involves a detailed comparison of the test cells. To facilitate this, the measurements at the AtC cell were conducted initially. From this data, gas production and water consumption can be calculated using equations (1)–(3). For this purpose, precise temperature and current data for each segment were obtained from the corresponding measurements in the AtC cell. As the overall current is provided to the end plates of the segmented cell, all segments are operated at the same voltage. Thus, deviations in the local current density relative to the average setpoint value have to be expected. The fluctuations in local current density are quite comparable for each current density, with variations within the range of +6% to −9%, and the most significant deviations observed in segments 5 and 6. Consequently, four segments, namely segments 1, 4, 7, and 10, were selected for further analysis, as they are equally spaced. The temperature profile shows that a higher average current density result in an increased cell temperature due to self-heating effects (54 °C at 1 A cm^{-2} and up to 71 °C at 5 A cm^{-2}). For the lower current densities, the temperature remains relatively stable along the channel, whereas at the highest current density of 5 A cm^{-2}, there is a noticeable trend of increasing temperature along the channel by 6 K from first to last segment. The measurement data of current and temperature of the AtC cell, along with the calculated values for the incremental cell, are summarized in Table SI1.

3.4. Single segment comparison

The subsequent step involves conducting the measurement under identical conditions within the incremental cell. The results are illustrated in Fig. 7. A comparison is made among three distinct current densities, specifically 1 A cm^{-2}, 3 A cm^{-2}, and 5 A cm^{-2}. The selection of higher current densities was deliberate, as lower current densities are unlikely to produce significant variations along the gas channel due to minimal gas production. In Fig. 7 a) and b) the Nyquist plot and DRT presentation at 1 A cm^{-2} are respectively depicted for four different segments. The original data from the AtC cell are represented by solid lines, whereas the comparative data from the incremental cell are shown using dotted lines. The Nyquist plot is presented without the HFR component to facilitate better comparison, given the differences in ohmic resistance between the cells as discussed previously. The results at 1 A cm^{-2} demonstrate remarkable agreement between both test cells. The polarization resistance measured in the incremental cell is

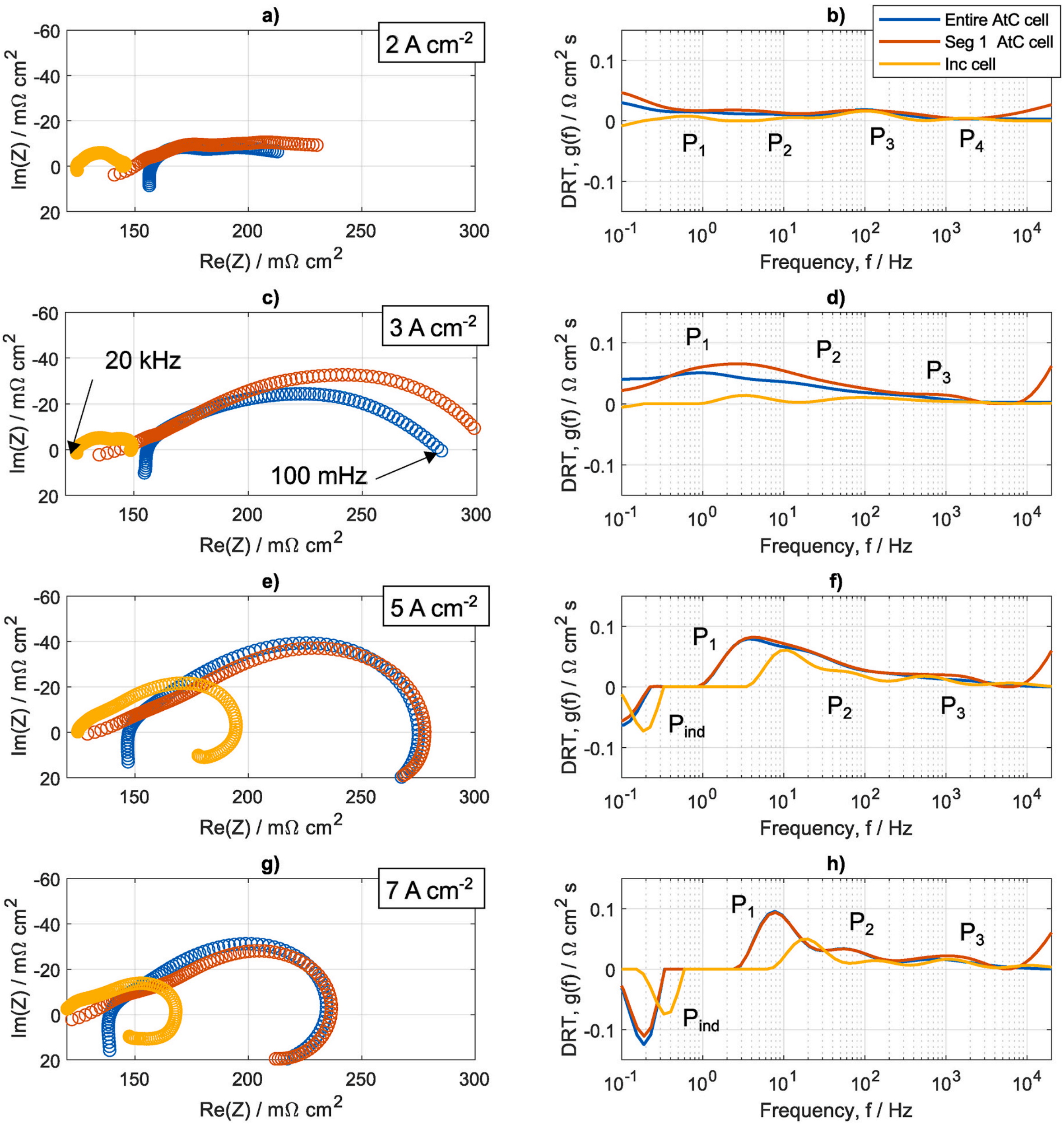

Fig. 6. Test cell comparison at high current densities of a), b) 2 A cm^{-2}, c) and d) 3 A cm^{-2}, e) and f) 5 A cm^{-2}, and g) and h) 7 A cm^{-2} at 60 °C, 0 bar and water flow rates of 10 mL min^{-1} cm^{-2} for the Inc cell and 5 mL min^{-1} cm^{-2} for the AtC cell.

marginally lower than that observed in the AtC cell. The DRT analysis reveals a consistent main peak P$_3$ at the same frequency across both measurements, which, according to Refs. [20], [22], [24], is attributable to charge transfer kinetics. The data from the AtC cell displays no definitive trend among the different segments, making it challenging to compare individual segments directly.

At 3 A cm^{-2} in Fig. 6 c) and 6 d), a significant disparity is observed between the AtC and incremental cell results. The AtC cell exhibits markedly higher polarization resistance relative to the incremental cell. In the DRT analysis, it is evident that this difference stems from processes in the low-frequency domain P$_1$ and P$_2$, which are associated with mass transport phenomena. The variations among the different segments of the AtC cell originate from differing effective currents within these segments. Conversely, the incremental cell does not replicate this trend; instead, it displays the expected increase in low-frequency mass transport processes with higher gas flow rates.

At 5 A cm^{-2} in Fig. 6 e) and 6 f), the process patterns realign more closely. Although the polarization resistance of the AtC cell remains higher than that of the incremental cell, the DRT shows peaks appearing within comparable frequency ranges across the different cells. In this current density region, the inductive loop, visible as P$_{ind}$ in the DRT, starts to form and is overlapping with the mass transport related losses.

Possible reasons for the significantly higher polarization resistance observed for the AtC cell compared to the incremental cell, particularly in the intermediate current density range of 2–3 A cm^{-2}, are discussed in the following. It should be emphasized that the origin of this behavior cannot be identified conclusively based on the present data and that multiple, potentially overlapping effects may contribute.

A first possible explanation is cation contamination originating from the CCM or auxiliary cell components. Such contamination is known to lead to a characteristic S-shaped distortion of polarization curves, as observed for the AtC cell in Fig. 4 between 2 and 3 A cm^{-2}. Padgett et al. [36] demonstrated that cation contamination can induce losses that resemble mass-transport limitations, causing an upward curvature of the

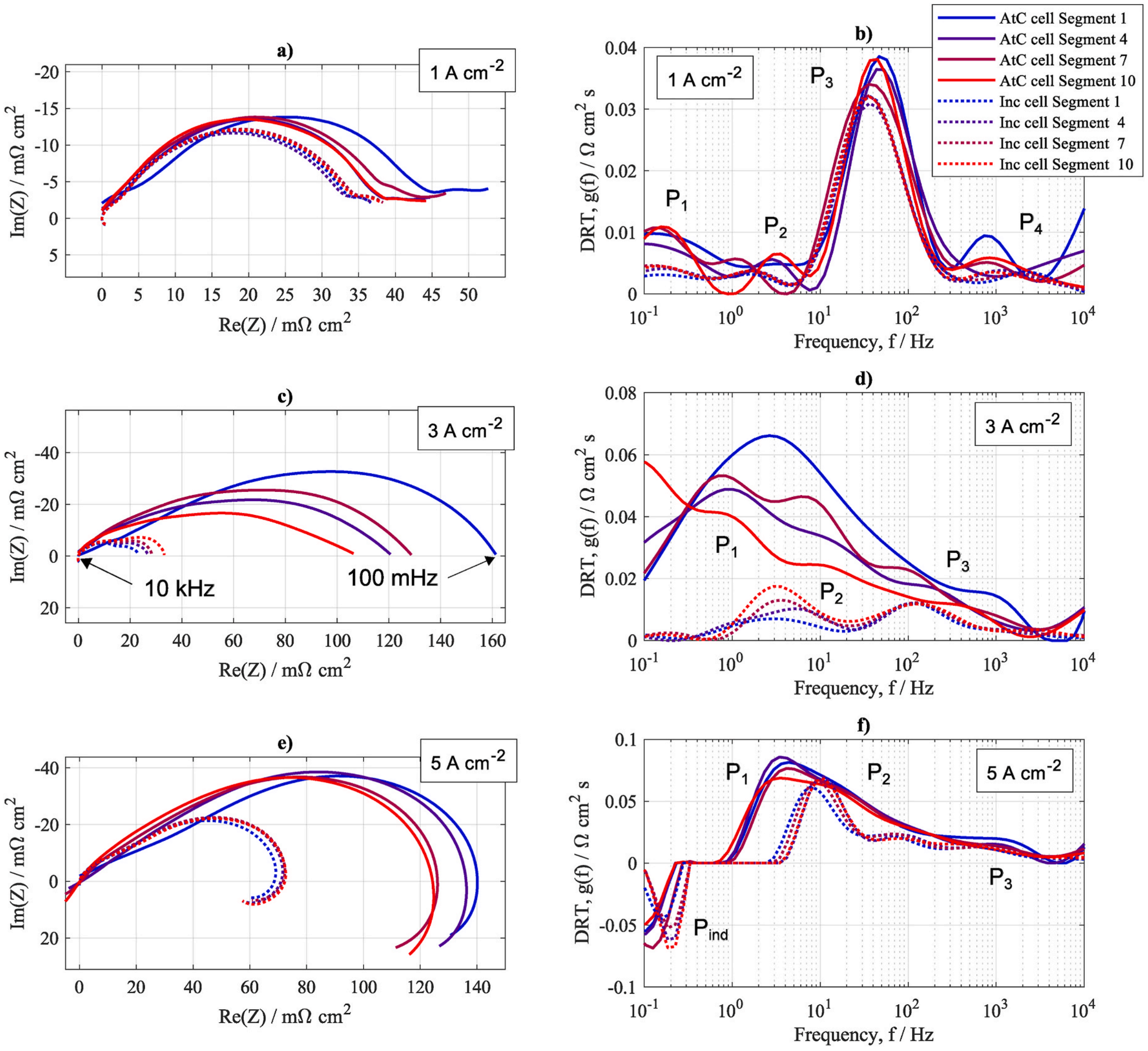

Fig. 7. Single segment comparison at a), b) 1 A cm-2, c), d) 3 A cm-2, and e), f) 5 A cm-2 with Nyquist plot on the left and DRT presentation on the right at 60 °C, 0 bar and water flow rates of 210 mL min^{-1} for the Inc cell and 300 mL min^{-1} for the AtC cell.

polarization curve in the medium current density regime, which levels off again at higher current densities due to changes in the HER mechanism. While this represents a plausible explanation, it cannot be stated with certainty that contamination is the dominant cause of the behavior observed here. Nevertheless, such effects may be more pronounced in the AtC configuration due to its larger water circuit and higher material complexity compared to the incremental cell, thereby increasing the susceptibility to unintended ionic impurities.

A second contributing factor may arise from transport limitations at the catalyst layer–PTL interface. As shown by Hensle et al. [16], the interaction between CCM properties and PTL structure can strongly influence mass transport behavior. In that work, low catalyst loadings in combination with the employed PTL resulted in increased transport resistances at higher current densities. Since the AtC and incremental cells investigated in this study employ comparable CCMs and PTLs, similar interfacial transport effects may occur. In the AtC cell, such effects could be aggravated by less homogeneous compression across individual segments, which may locally alter contact conditions and effective transport pathways.

In this context, it should be noted that the AtC cell employs only global mechanical compression, applied to the full cell assembly, rather than local or segment-resolved compression. No sensors or diagnostic tools are integrated in this cell to directly measure or verify the compression state of individual segments operando. As a result, local variations in compression cannot be excluded and an inhomogeneous contact between PTL and catalyst layer may deactivate parts of a segment area and thus contribute to locally increased polarization resistances. Such effects are absent in the incremental cell, where a single, well-defined active area and contact configuration are present.

Furthermore, in-plane transport effects may play a role in the segmented cell. Due to the longer segments and the segmentation of the PTL, lateral redistribution of reactants and removal of product gases can be hindered. Gas accumulation in upstream regions of a segment may partially block downstream active areas within the same segment, effectively increasing the mass transport resistance. These in-plane effects are avoided in the incremental cell, owing to its shorter active length and the use of a single PTL element without segmentation.

Overall, these considerations illustrate that a direct quantitative comparison between AtC and incremental cells remains challenging. Beyond quantitative deviations, the results also exhibit qualitative differences, as reflected by differing trends along the flow channel between the incremental and AtC cells. Consequently, even qualitative comparisons between both cell concepts should be interpreted with care. In the AtC configuration, segment-specific inhomogeneities—such as compression variations, interfacial transport resistances, or possible contamination effects—may overlay the along-the-channel phenomena investigated in this study. We therefore conclude that, within the scope of this study, the incremental cell results provide a more reliable basis compared to the AtC cell results. The experiments presented here were conducted under near-system-relevant conditions with relatively high water flow rates, resulting in small gradients along the flow channel. Alternative experimental strategies that deliberately enhance segment differentiation, such as operation at very low water flow rates as discussed in Ref. [19], could help to further disentangle along-the-channel effects from setup-specific inhomogeneities in future work.

4. Conclusion

This study presents investigations into a largely unexplored domain, specifically the mimicking of gas production in large cells and the impact of spatially differing water to gas ratios utilizing a more accessible laboratory-scale setup. Initially, varying amounts of product gases are introduced either to both the cathode and anode sides or solely to one side. This approach demonstrated that the influence of gas mixing on both the ohmic and polarization resistance is associated with the introduction of hydrogen to the cathode side. Conversely, the mixing of oxygen into the anode stream appears to have no significant effect at the two evaluated current densities of 0.1 A cm^{-2} and 2 A cm^{-2}. The gas mixing experiments indicate that higher gas quantities lead to an increase in ohmic resistance, most probably related to membrane dehydration via the cathode side. Additionally, at low current densities, a reduction in polarization resistance is observed when gas is supplied, indicating improved activation behavior. This effect can be attributed to the hydrogen supplied at the cathode side.

In the further analysis of this study, a comparison between an incremental cell and a segmented along the channel cell is made. Initial comparisons of the entire cell results reveal good agreement and consistent trends for a current density variation. By precisely replicating the conditions of the AtC measurement from measurement result, a comparison in the behavior of individual segments with the incremental cell is made. However, this aspect requires further refinement. Current limitations prevent accurate replication of individual segments, as the differences are too substantial and no clear distinctions are observed in the AtC measurements alongside the active area. Consequently, additional investigations under alternative conditions (e.g., reduced water flow rate) would be beneficial to determine if the replication can be improved.

Declaration of generative AI and AI-assisted technologies in the writing process

During the preparation of this work the authors used Grammarly (https://app.grammarly.com) in order to improve the academic tone and accuracy of language, including grammatical structure, punctuation, and vocabulary. After using this tool, the authors reviewed and edited the content as needed and take full responsibility for the content of the published article.

CRediT authorship contribution statement

Debora Brinker: Conceptualization, Data curation, Investigation, Methodology, Software, Validation, Visualization, Writing – original draft. **Niklas Hensle:** Conceptualization, Data curation, Investigation, Methodology, Resources, Writing – review & editing. **Christin Büsching:** Investigation, Methodology, Software. **David Breuninger:** Investigation, Methodology, Software. **Tom Smolinka:** Funding acquisition, Resources, Supervision. **André Weber:** Conceptualization, Funding acquisition, Supervision, Writing – review & editing.

Declaration of competing interest

The authors declare that they have no known competing financial interests or personal relationships that could have appeared to influence the work reported in this paper.

Acknowledgment

The authors gratefully acknowledge funding from the Federal Ministry of Research, Technology and Space, Germany (BMFTR 03HY103C and 03HY103F). We thank Schaeffler Technologies AG & Co. KG, Germany for the collaboration.

Appendix A. Supplementary data

Supplementary data to this article can be found online at https://doi.org/10.1016/j.jpowsour.2026.240293.

Data availability

The data presented in the manuscript are openly available in the KITopen repository at https://doi.org/10.35097/40ftt1bc5gdg2cz6.

References

[1] A. Franco, C. Giovannini, Recent and future advances in water electrolysis for green hydrogen generation: critical analysis and perspectives, Sustainability 15 (24) (Jan. 2023) 16917, https://doi.org/10.3390/su152416917.

[2] I. Elegbeleye, O. Oguntona, F. Elegbeleye, Green hydrogen: pathway to net zero green house gas emission and global climate change mitigation, Hydrogen 6 (2) (Jun. 2025) 29, https://doi.org/10.3390/hydrogen6020029.

[3] P.K. Pathak, A.K. Yadav, I. Kamwa, Green hydrogen: a strategic energy vector for achieving net-zero emissions by 2050, Sustain. Energy Fuels 9 (19) (Sep. 2025) 5218–5226, https://doi.org/10.1039/D5SE00902B.

[4] A. Mohammadi, M. Mehrpooya, A comprehensive review on coupling different types of electrolyzer to renewable energy sources, Energy 158 (2018) 632–655.

[5] P. Lettenmeier, R. Wang, R. Abouatallah, F. Burggraf, A.S. Gago, K.A. Friedrich, Proton exchange membrane electrolyzer systems operating dynamically at high current densities, ECS Trans. 72 (23) (2016) 11.

[6] V.M. Lopez, H. Ziar, J.W. Haverkort, M. Zeman, O. Isabella, Dynamic operation of water electrolyzers: a review for applications in photovoltaic systems integration, Renew. Sustain. Energy Rev. 182 (2023) 113407, https://doi.org/10.1016/j.rser.2023.113407.

[7] M.M. Rashid, M.K. Al Mesfer, H. Naseem, M. Danish, Hydrogen production by water electrolysis: a review of alkaline water electrolysis, PEM water electrolysis and high temperature water electrolysis, Int. J. Eng. Adv. Technol. 4 (3) (Jan. 2015) 80–93.

[8] C.R. Wang, et al., Proton exchange membrane (PEM) water electrolysis: cell-level considerations for gigawatt-scale deployment, Chem. Rev. 125 (3) (Feb. 2025) 1257–1302, https://doi.org/10.1021/acs.chemrev.3c00904.

[9] P. Lettenmeier, et al., Durable membrane electrode assemblies for proton exchange membrane electrolyzer systems operating at high current densities, Electrochim. Acta 210 (Jan. 2016) 502–511, https://doi.org/10.1016/j.electacta.2016.04.164.

[10] A. Villagra, P. Millet, An analysis of PEM water electrolysis cells operating at elevated current densities, Int. J. Hydrogen Energy 44 (20) (Apr. 2019) 9708–9717, https://doi.org/10.1016/j.ijhydene.2018.11.179.

[11] A. Martin, P. Trinke, B. Bensmann, R. Hanke-Rauschenbach, Hydrogen crossover in PEM water electrolysis at current densities up to 10 A cm^{-2}, J. Electrochem. Soc. 169 (9) (Sep. 2022) 094507, https://doi.org/10.1149/1945-7111/ac908c.

[12] Y. Li, et al., In-situ investigation of bubble dynamics and two-phase flow in proton exchange membrane electrolyzer cells, Int. J. Hydrogen Energy 43 (24) (Jan. 2018) 24, https://doi.org/10.1016/j.ijhydene.2018.05.006.

[13] J.O. Majasan, J.I.S. Cho, I. Dedigama, D. Tsaoulidis, P. Shearing, D.J.L. Brett, Two-phase flow behaviour and performance of polymer electrolyte membrane electrolysers: electrochemical and optical characterisation, Int. J. Hydrogen Energy 43 (33) (Jan. 2018) 33, https://doi.org/10.1016/j.ijhydene.2018.07.003.

[14] H. Ito, et al., Effect of flow regime of circulating water on a proton exchange membrane electrolyzer, Int. J. Hydrogen Energy 35 (18) (Jan. 2010) 18, https://doi.org/10.1016/j.ijhydene.2010.06.103.

[15] N. Hensle, S. Metz, A. Weber, T. Smolinka, A segmented along the channel test cell for locally resolved analysis at high current densities in PEM water electrolysis, J. Electrochem. Soc. 171 (11) (Nov. 2024) 114510, https://doi.org/10.1149/1945-7111/ad9064.

[16] N. Hensle, et al., Understanding the cell performance along the channel for industrial PEM water electrolysis operation, ACS Appl. Energy Mater. 8 (11) (Jun. 2025) 7107–7124, https://doi.org/10.1021/acsaem.5c00505.

[17] C. Immerz, B. Bensmann, P. Trinke, M. Suermann, R. Hanke-Rauschenbach, Local current density and electrochemical impedance measurements within 50 cm single-channel PEM electrolysis cell, J. Electrochem. Soc. 165 (16) (Jan. 2018) 16, https://doi.org/10.1149/2.0411816jes.

[18] J. Parra-Restrepo, et al., Influence of the porous transport layer properties on the mass and charge transfer in a segmented PEM electrolyzer, Int. J. Hydrogen Energy 45 (15) (Jan. 2020) 15, https://doi.org/10.1016/j.ijhydene.2020.01.100.

[19] N. Hensle, T. Lickert, N. Winterholler, T. Smolinka, A. Weber, Water starvation phenomena in a segmented along the channel PEM water electrolysis cell, J. Power Sources 654 (Oct. 2025) 237865, https://doi.org/10.1016/j.jpowsour.2025.237865.

[20] J. Zuo, N.Y. Steiner, Z. Li, D. Hissel, Quantitative investigation of internal polarization in a proton exchange membrane water electrolyzer stack using distribution of relaxation times, Appl. Energy 386 (May 2025) 125543, https://doi.org/10.1016/j.apenergy.2025.125543.

[21] J. Zuo, N.Y. Steiner, Z. Li, D. Hissel, Interpreting full-frequency impedance spectrum for PEM electrolyzers: distribution of relaxation times-based modeling, Appl. Energy 394 (Sep. 2025) 126185, https://doi.org/10.1016/j.apenergy.2025.126185.

[22] A.-L. Chan, H. Yu, K.S. Reeves, S.M. Alia, Identifying electrochemical processes by distribution of relaxation times in proton exchange membrane electrolyzers, J. Power Sources 628 (Feb. 2025) 235850, https://doi.org/10.1016/j.jpowsour.2024.235850.

[23] Y. Li, et al., Application of distribution of relaxation times method in polymer electrolyte membrane water electrolyzer, Chem. Eng. J. 451 (Jan. 2023) 138327, https://doi.org/10.1016/j.cej.2022.138327.

[24] D. Brinker, et al., Distribution of relaxation times-based impedance analysis of incremental PEM water electrolysis cells, Int. J. Hydrogen Energy 218 (Mar. 2026) 154048, https://doi.org/10.1016/j.ijhydene.2026.154048.

[25] T. Lickert, et al., On the influence of the anodic porous transport layer on PEM electrolysis performance at high current densities, Int. J. Hydrogen Energy 45 (11) (Jan. 2020) 11, https://doi.org/10.1016/j.ijhydene.2019.12.204.

[26] T. Lickert, et al., Advances in benchmarking and round robin testing for PEM water electrolysis: reference protocol and hardware, Appl. Energy 352 (Jan. 2023) 121898, https://doi.org/10.1016/j.apenergy.2023.121898.

[27] M. Maier, K. Smith, J. Dodwell, G. Hinds, P.R. Shearing, D.J.L. Brett, Mass transport in PEM water electrolysers: a review, Int. J. Hydrogen Energy 47 (1) (Jan. 2022) 30–56, https://doi.org/10.1016/j.ijhydene.2021.10.013.

[28] H.-S. Shin, B.S. Oh, Water transport according to temperature and current in PEM water electrolyzer, Int. J. Hydrogen Energy 45 (1) (Jan. 2020) 56–63, https://doi.org/10.1016/j.ijhydene.2019.10.209.

[29] T. Berning, On the nature of electro-osmotic drag, Energies 13 (18) (Sep. 2020) 4726, https://doi.org/10.3390/en13184726.

[30] M. Schönleber, D. Klotz, E. Ivers-Tiffée, A method for improving the robustness of linear kramers-kronig validity tests, Electrochim. Acta 131 (Jan. 2014) 20–27, https://doi.org/10.1016/j.electacta.2014.01.034.

[31] E. Ivers-Tiffée, A. Weber, Evaluation of electrochemical impedance spectra by the distribution of relaxation times, J. Ceram. Soc. Jpn. 125 (4) (Jan. 2017) 125 [4].

[32] A. Schiefer, M. Heinzmann, A. Weber, Inductive low-frequency processes in PEMFC-Impedance spectra, Fuel Cells 20 (4) (Jan. 2020) 4, https://doi.org/10.1002/fuce.201900212.

[33] A.N. Tikhonov, A. Gončarskij, V.V. Stepanov, A.G. Jagola (Eds.), Numerical Methods for the Solution of Ill-Posed Problems, Springer eBook Collection Mathematics and Statistics, vol.328, Springer, Dordrecht, 1995, https://doi.org/10.1007/978-94-015-8480-7 vol. 328.

[34] K.J. Kabamba, T. Binninger, B. Bensmann, R. Mohamed, Kinetic origin of the sub-nernstian cell voltage response in pressurised PEM water electrolysis, Int. J. Hydrogen Energy 226 (Apr. 2026) 154454, https://doi.org/10.1016/j.ijhydene.2026.154454.

[35] D. Brinker, et al., Inductive loops in impedance spectra of PEM water electrolyzers, J. Power Sources 622 (Dec. 2024) 235375, https://doi.org/10.1016/j.jpowsour.2024.235375.

[36] E. Padgett, et al., Performance losses and current-driven recovery from cation contaminants in PEM water electrolysis, J. Electrochem. Soc. 171 (6) (Jun. 2024) 064510, https://doi.org/10.1149/1945-7111/ad576b.